



Aero-structural Analysis of a Scramjet Technology Demonstrator Designed to Operate at an Altitude of 23 km at Mach 5.8

Paulo César de Oliveira Júnior¹ · João Carlos Arantes Costa Júnior² · Paulo Gilberto de Paula Toro^{1,2}

Received: 17 January 2024 / Accepted: 24 June 2024

© The Author(s), under exclusive licence to Springer Nature B.V. 2024, corrected publication 2024

Abstract

Aerodynamic and structural analysis was conducted for a generic supersonic combustion demonstrator designed to operate under flight conditions at an altitude of 23 km and a speed corresponding to Mach number 5.8. Optimization methodologies were applied to the compression section of the model to ensure the required temperature and Mach number conditions at the combustion chamber entrance for the spontaneous combustion of hydrogen fuel, as well as to the expansion section to meet the Brayton thermodynamic cycle. In the aerodynamic analysis, both analytical and numerical approaches were considered for cases without fuel injection and with fuel burning, treating air as a calorically perfect gas without viscous effects. In the structural analysis, only the case with fuel burning was evaluated due to its higher structural demands. Additionally, cases with different plate thicknesses (6 mm, 4 mm, 3 mm, and 2.5 mm) were considered, and the components of the scramjet consisted of Stainless Steel 304 (beams and ribs), Aluminum 7075 (side panels and ramps), Inconel 718, or Tungsten (leading edges and combustion chamber entrance). The results of the aerodynamic numerical simulation demonstrated that the designed scramjet was capable of meeting both on-lip and on-corner shock conditions, ensuring maximum atmospheric air capture. In the structural numerical simulation, for sheets thicker than 2.5 mm, the maximum equivalent von Mises stress in the structure was lower than the yield stress of the materials used, indicating that the deformations were within the elastic regime and thus reversible.

Keywords Supersonic combustion · Scramjet · Hypersonic airbreathing propulsion · Aerodynamic analysis · Structural analysis · Aero-structural numerical simulation

✉ Paulo César de Oliveira Júnior
pauoloc@gmail.com

¹ Instituto Tecnológico de Aeronáutica (ITA), Praça Marechal Eduardo Gomes, 50, Vila das Acácias, São José dos Campos 12228-900, São Paulo, Brazil

² Universidade Federal do Rio Grande do Norte (UFRN), Av. Senador Salgado Filho, 3000, Campus Universitário Lagoa Nova, Natal 59078-900, Rio Grande do Norte, Brazil

1 Introduction

Since the mid-1960s, NASA has been developing tools to design and test a hydrogen-powered and cooled scramjet for scramjet cycle efficiency and structural integrity. Since the early 1970s, NASA has designed and demonstrated, in a wind tunnel, a fuselage-integrated scramjet “flow path” with fixed geometry capable of propelling a hypersonic vehicle from Mach numbers 4 to 7. In mid-1980s, NASA started the program of the most ambitious project involving airbreathing propulsion called NASP (National Aero-Space Plane), whose objective was to design a reusable, single-stage vehicle powered by a multi-cycle propulsion system. Basically, the vehicle would take-off from an airport runway like a conventional aircraft (turbine), accelerate to supersonic (ramjet) and hypersonic (scramjet) speeds. The scramjet propulsion would be used until the aerospace vehicle reaches low Earth orbit, and then it would return for landing at a conventional airport (Volad et al. 2006).

In 1993, the NASP consortium conducted a comprehensive assessment encompassing cost and risk analysis. This evaluation brought to light challenges associated with aerodynamic heating and the utilization of nascent technologies within the project, ultimately leading to the program’s discontinuation in 1995. Nevertheless, this setback yielded a substantial corpus of valuable data derived from research on ramjet (subsonic combustion) and scramjet (supersonic combustion) technologies. These invaluable findings served as the foundation for the subsequent, more modest Hyper-X supersonic combustion demonstrator project, culminating in the development of the X-43 demonstrator in 1996 (McClinton 2006).

More than a decade later, major technological and scientific challenges remain, such as the fact that the thermal loads on the vehicle structure increase with the square of the cruising speed. In this context, the aero-thermo-elastic problem was a critical area in hypersonic flight, due to severe aerodynamic heating that can cause structural deformation as well as melting of the leading edges. Particularly for scramjets operating at low altitudes, the combined effect of dynamic pressures and internal thermal stresses must be considered (Ho and Paull 2006).

Flying in Earth’s dense atmosphere, hypersonic vehicles are exposed to a harsh environment, which can severely damage the structure. Thus, it is essential that they be designed to withstand the severe conditions of hypersonic flight, resulting from aerodynamic and thermal loads, implying the need to estimate the aerodynamic heating and predict the behavior of the vehicle structure. Especially for reusable vehicles, aero-thermo-elasticity is of particular interest, due to the cumulative effects of residual stresses, creep and material degradation associated with high temperatures, which compromise the useful life of the aircraft (Ho and Paull 2006; Sziroczak and Smith 2016).

In structures for high-speed flight vehicles, depending on the flight conditions, thermal stresses can be significant and temperature variations can induce dynamic instabilities. The ability to provide meaningful analytical predictions of this behavior requires a unified thermo-structural approach that results in a mathematical model that has some complexities. The effectiveness of the finite element approach applied to field problems makes it a natural candidate for solving this problem. However, the numerical precision of finite element solutions is linked to the degree of discretization of the analyzed domain, and sometimes results in substantial increases in computational requirements (Tavares and Hajela 1992; Gopinath et al. 2019).

Typically, for the simplification of the aero-elastic problem, “weak” couplings between the different disciplines that constitute the field of aero-thermo-elasticity (aerodynamic

heating, aerodynamic pressure, elastic forces and inertial forces) are neglected, as well as the effect of aerodynamic pressure in aerodynamic heating (Culler and McNamara 2011; Tirtay and Boyce 2012; Scigliano and Gardi 2013; Carandente and Scigliano 2016). Basically, this simplification is based on the following assumptions: (1) the thermodynamic coupling between heat generation and elastic deformation is negligible; (2) the aeroelastic coupling is small; (3) the static aero-elastic coupling, referring to static elastic deflections due to steady-state pressure and thermal load, is not sufficient to change the temperature distribution of the reference condition. However, under conditions where these assumptions fail, it is necessary to update the aerodynamic heating conditions based on the structural deformation from the feedback from the aeroelastic solution to the aerothermal solution (Culler and McNamara 2011).

In this paper, a preliminary design of a supersonic combustion demonstrator is presented, based on aero-structural analysis, considering air as a calorically perfect gas and without viscous effects, under atmospheric flight conditions at a geometric altitude of 23 km and a velocity of 1723 m/s. The compression section is proposed, optimized to provide the necessary temperature and Mach number conditions for the combustion of hydrogen fuel. In this regard, the aerodynamic analysis of the proposed model is developed, and subsequently, the effects of the aerodynamic load on the scramjet structure are evaluated.

2 Scramjet Characteristics

To gain a better understanding of the characteristics of the scramjet, we employed the nomenclature as elucidated by Heiser and Pratt (1994). In Fig. 1, conventional terminology was applied to a planar geometry consisting of three compression ramps, symmetric about

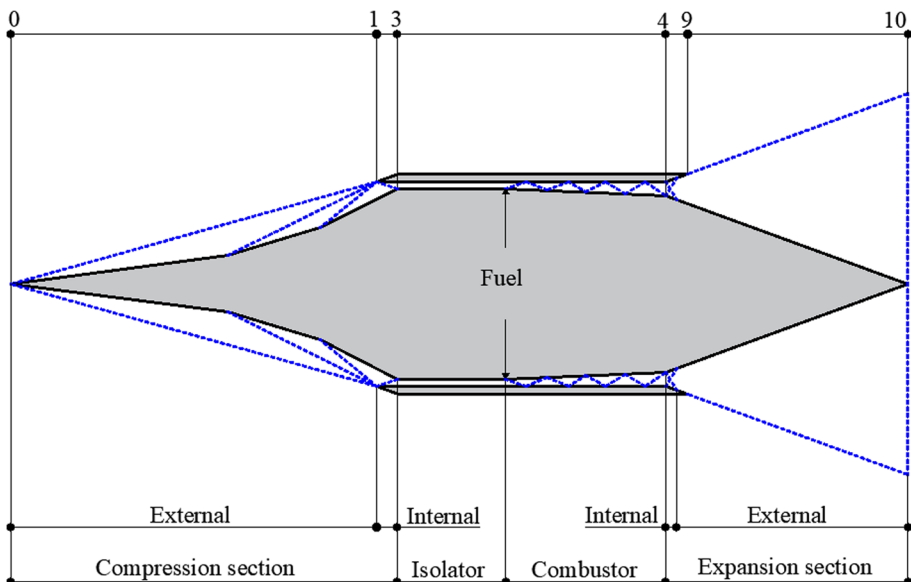


Fig. 1 Terminology used in scramjets

Fig. 2 Brayton thermodynamic cycle for scramjets (Carneiro et al. 2023)

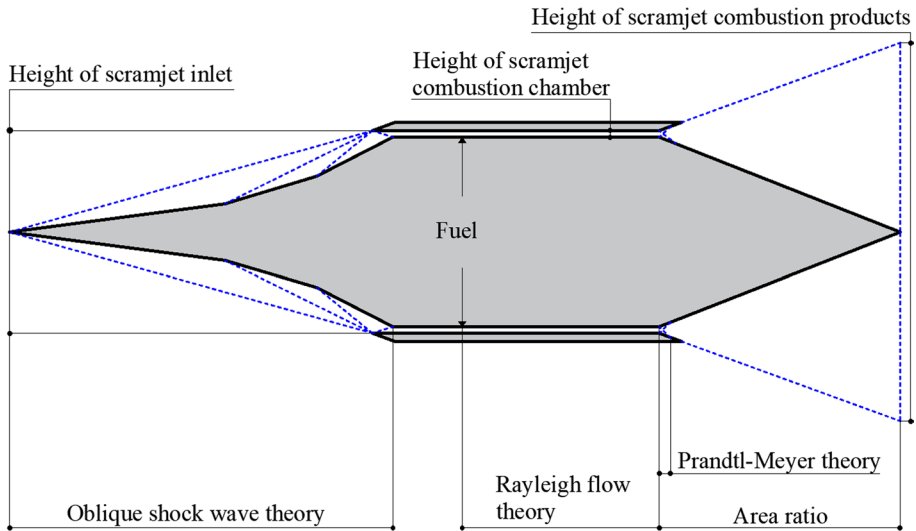
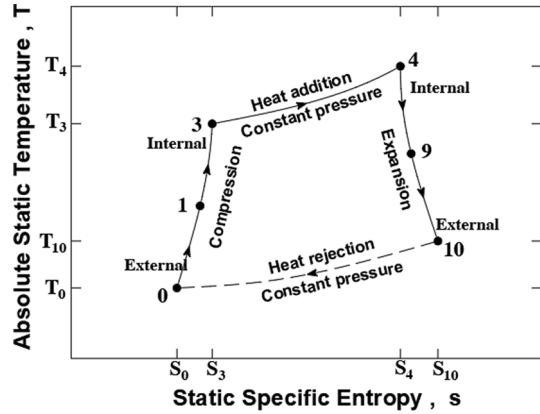


Fig. 3 Theories applied in scramjets, adapted from Carneiro et al. (2022)

a plane passing through the leading and trailing edges. Each symmetrical section represents a waverider with a wedge-derived flat inlet configuration.

As stated by Heiser and Pratt (1994), scramjets operate according to the thermodynamic Brayton cycle (Fig. 2), to generate thrust. It should be noted that the thermodynamic cycle is open because there is no recirculation of air in the system, since the products of combustion (expansion gases) are discharged directly into the atmosphere.

The adiabatic compression section is formed by the external compression section (stations 0 to 1), where incident oblique shock waves are established, and the internal compression section (stations 1 to 3), where a reflected oblique shock wave is established (Figs. 1, 2, 3). The combustion section (stations 3 to 4) is composed of an isolator, a region of constant area and pressure (from station 3 to fuel injection), and the combustor (from fuel injection to station 4), following the thermodynamic Brayton cycle, maintaining constant pressure and variable area during the fuel injection to station 4 interval (Figs. 1, 2). The

isolator is employed to standardize the flow of atmospheric air captured by the compression section, and fuel is injected at the beginning of the combustor, under constant pressure and variable area conditions. The adiabatic expansion section is comprised of the internal expansion section (stations 4 to 9) and the external expansion section (stations 9 to 10) (Figs. 1, 2, 3).

The oblique shock wave theory and the Prandtl–Meyer theory coupled with the area ratio can be applied to the compression and expansion sections, respectively. For simplification, the combustion of hydrogen with atmospheric air at supersonic speeds can be modeled using the one-dimensional flow with heat addition (Rayleigh theory), but without considering the addition of fuel mass. This is due to a constant area, resulting in an increase in pressure (Fig. 3) (Anderson Jr 2003).

According to Weber and MacKay (1958), the scramjet cycle can be conveniently illustrated by a temperature entropy diagram. As atmospheric air is decelerated to a lower Mach number, but still supersonic, it is possible to demonstrate that the increase in entropy is directly related to a loss of total pressure, so that the Rayleigh line can be used to represent the process of heat addition in a constant area and frictionless duct.

Note that for the variable area combustor (Fig. 1), the Brayton thermodynamic cycle establishes constant pressure and an increase in temperature from T_3 to T_4 (Fig. 2). To determine the hydrogen fuel combustion analytically, Rayleigh's theory is employed (Fig. 3). In this case, we have heat addition without the addition of fuel mass, consequently constant area for the combustor, resulting in pressure increase.

The oblique shock waves established in the external compression section of the scramjet are responsible for the compression and deceleration of atmospheric air, providing supersonic velocities at the appropriate temperature (higher than the ignition temperature of the fuel) at the combustion chamber inlet (Heiser and Pratt 1994).

Suitable temperature and supersonic atmospheric air velocity conditions allow for its mixture with the fuel (hydrogen-air mixture) and spontaneous combustion within the combustion chamber. Due to the limitations of the scramjet in not generating thrust from rest or at supersonic speeds, an acceleration system (typically a rocket engine) is used to accelerate the scramjet to the operating conditions for supersonic combustion, generating sufficient thrust for the aircraft to continue flying in Earth's atmosphere (Carneiro et al. 2022).

In the scramjet, the frontal (compression) section is responsible for capturing atmospheric air, compressing and decelerating it to the proper conditions at the combustion chamber entrance to burn the hydrogen-air mixture at supersonic velocity. The rear (expansion) section contributes to thrust generation as well as the integration between the booster vehicle (rocket engine) and the airbreathing propulsion system, working together for supersonic combustion.

3 Scramjet Flowpath Design Methodology

Considering the flight conditions at a geometric altitude of 23 km and a speed of 1723 m/s (Mach number 5.8), provided by the accelerator vehicle based on the Brazilian rocket engines S30 and S31, and assuming the atmospheric air as a calorically perfect gas ($\gamma=1.4$) and no viscous effects from the scramjet leading-to-trailing edges, which is suitable for preliminary scramjet design, established a simple methodology and fast to obtaining of results.

Table 1 Thermodynamic properties of atmospheric air at an altitude of 23 km, adapted from NASA (1976)

Z (km)	p (Pa)	T (K)	ρ (kg/m ³)	a (m/s)
23	3466.86	219.57	0.05501	297.05

Table 2 Fuels commonly used in scramjets, adapted from Araújo et al. (2021)

Fuel	T^{ign} (K)	f_{st}	ρ (kg/m ³)	γ	R [J/(kg•K)]
Hydrogen (H ₂)	845.15	0.0291	70.7	1.405	4124
Methane (CH ₄)	810.15	0.0582	423	1.303	518.2
Ethane (C ₂ H ₆)	745.15	0.0624	–	1.188	276.5
Octane (C ₈ H ₁₈)	479.15	0.0664	703	1.044	72.79
JP-7 (C ₁₂ H ₂₅)	514.15	0.0674	790	–	–

Coupled with the S30 and S31 rocket engines VSB-30, the scramjet was positioned at the upper end of the S31 rocket engine. The scramjet was inscribed in the payload envelope of the rocket engine whose diameter is 428 mm. The accelerator vehicle provides acceleration of 78,480 mm/s² needed for the scramjet to reach its operating conditions at 23 km altitude and velocity of 1723 m/s.

Atmospheric air at an altitude (Z) of 23 km was modeled considering the standard 1976 United States atmosphere (NASA 1976) (Table 1). The Mach number of 5.8 is the result of scramjet flight speed (u) of 1723 m/s at 23 km altitude where the sound speed (a) is 297.05 m/s.

The aerodynamic design of the scramjet was developed analytically, considering criteria and optimization in the compression and expansion sections, in addition to approaches no fuel injection (power-off) and with fuel burning (power-on). Numerical flow simulations make possible to compare the analytical results and verify the optimization criteria used. Finally, the analysis of the structure was developed for the case with fuel combustion, considering aerodynamic pressure load from the analytical analysis, validated from the aerodynamic numerical analysis.

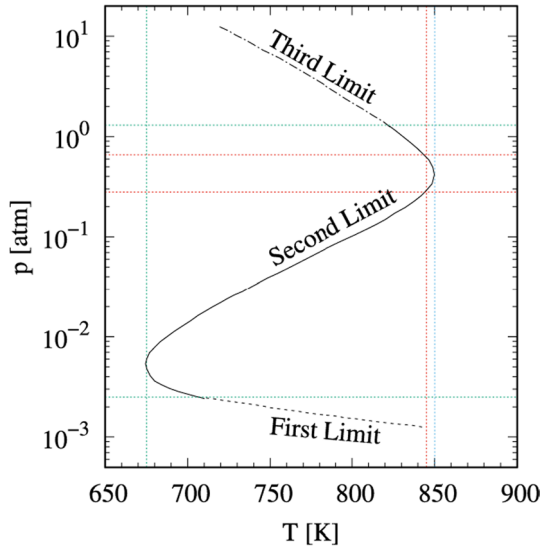
3.1 Conditions Required at the Combustion Chamber Entrance

In the scramjet, atmospheric air captured by the compression section and routed to the combustion chamber entrance must transfer sufficient heat to raise the fuel temperature to ignition temperature (T^{ign}) (Araújo et al. 2021).

In systems with airbreathing propulsion, depending on the purpose, hydrocarbons or hydrogen can be used as fuel. In the case of hydrogen gas, the molecular weight is lower (molecule with only two hydrogen atoms, Table 2), favoring the specific impulse (Bezerra et al. 2024).

On the ground, hydrogen must be pressurized at low temperature, around 300 K, with a pressure of 5 atm, and then loaded onto the scramjet before launch. The combustion of hydrogen depends on pressure at temperatures ranging from 670 to 850 K (Fig. 4). The ignition temperature of hydrogen is 845.15 K. Essentially, the pressure must be below 0.3 atm or above 0.7 atm (Sung et al. 2012).

Fig. 4 Explosion (combustion) limits for a stoichiometric hydrogen-air mixture in a closed vessel (Araújo et al. 2021)



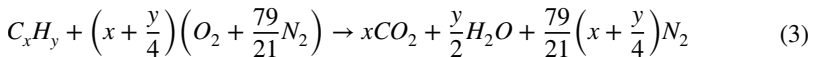
The zero law and the first law of thermodynamics were applied to define the energy balance of the mass flow entering the combustion chamber (atmospheric air) and the mass flow leaving the combustion chamber (air-hydrogen mixture) and, thus, determine the temperature at the combustion chamber entrance (T_3), Eq. (1), necessary to raise the hydrogen injection temperature (T^{inj}) (300 K) to the ignition temperature (845.15 K).

$$T_3 = f \cdot \frac{c_{p_{H_2}}}{c_{p_{air}}} \cdot (T_{H_2}^{ign} - T_{H_2}^{inj}) + T_{H_2}^{ign} \tag{1}$$

In Eq. (1), f is the fuel/air mass flow ratio, given by Eq. (2).

$$f = \frac{\dot{m}_{fuel}}{\dot{m}_{air}} \tag{2}$$

The products of the combustion of hydrocarbons C_xH_y or hydrogen H_2 with the constituents of atmospheric air (21% O_2 and 79% N_2) can be determined from the basic principles of chemical reactions, Eq. (3) (Heiser and Pratt 1994).



From the basic principles of chemical reactions, the stoichiometric mass ratio of fuel/air can be obtained by considering the atomic weights of the constituent elements ($H=1$, $C=12$, $N=14$, and $O=16$), Eq. (4), where x and y are the subscripts referring to carbon and hydrogen, respectively (Heiser and Pratt 1994).

$$f_{st} = \frac{36x + 3y}{103(4x + y)} \tag{4}$$

Heiser and Pratt (1994) define the equivalence ratio ϕ necessary to determine the fuel-to-air mass ratio for non-stoichiometric mixture case, Eq. (5). Thus, for stoichiometric

combustion, the equivalence ratio is unity ($\phi = 1$), and consequently, $f = f_{st}$. For non-stoichiometric mixture, two situations can occur: burning with excess air ($\phi < 1$) or burning with excess fuel ($\phi > 1$).

$$f = \phi f_{st} \tag{5}$$

The heat added to the flow comes from fuel combustion. Again, according to Rayleigh’s theory, there is heat addition without addition of fuel mass, consequently constant area and pressure increase. Thus, constant mass flow results in stoichiometric combustion. However, the equivalence ratio can be defined based on the added heat (q) and the lower heating value of the fuel (h_{pr}), Eq. (6).

$$q = \phi f_{st} h_{pr} \tag{6}$$

Finally, by the energy conservation law in the form of total temperature it is possible to determine the Mach number at the combustion chamber entrance (M_3), Eq. (7), considering that the total temperature was conserved in the scramjet compression section.

$$M_3 = \sqrt{\frac{2}{\gamma - 1} \cdot \left\{ \left[\left(1 + \frac{\gamma - 1}{2} \cdot M_0^2 \right) \cdot \frac{T_0}{T_3} \right] - 1 \right\}} \tag{7}$$

Thus, the conditions required at the scramjet combustion chamber entrance (station 3) depend only on the fuel used and the flight conditions (geometric altitude and Mach number, station 0), established for the scramjet design.

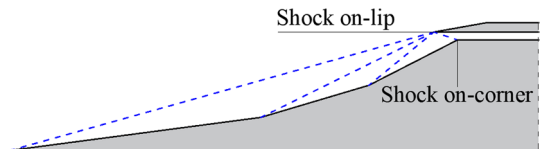
3.2 Optimization of the Compression Section

One of the earliest great projects for supersonic inlet was developed by Oswatitsch (1947), aiming to reduce supersonic airflow to subsonic speed in the combustion chamber of a missile. Using gas dynamics relationships and Lagrange multipliers to maximize the maximum total pressure recovery, it was observed that to improve compression efficiency, oblique shock waves must have the same strength (Oswatitsch criterion) (Prakash and Venkatasubbaiah 2012; Araújo et al. 2021).

The air mass captured by the compression section of the scramjet can be completely compressed and brought to the combustion chamber entrance. The maximum air capture (Fig. 5) occurs when all the incident shock waves on the compression section converge on the leading edge of the scramjet fairing (shock on-lip), and the reflected oblique shock wave impinges on the combustion chamber entrance (shock on-corner).

One of the relevant parameter for the performance of the compression section is the total pressure recovery (TPR), Eq. (8), which consists of the total pressure ratio (π) from the combustion chamber entrance (station 3) to the scramjet leading edge (station 0) in which the conditions are relative to free stream airflow.

Fig. 5 Maximum air captured by the scramjet compression section



$$TPR = \prod_{i=1}^n \pi_i = \frac{p_{T_3}}{p_{T_0}} = \frac{p_3}{p_0} \cdot \left(\frac{1 + \frac{\gamma-1}{2} \cdot M_3^2}{1 + \frac{\gamma-1}{2} \cdot M_0^2} \right)^{\frac{\gamma}{\gamma-1}} \tag{8}$$

The loss of total pressure has a direct influence on thrust reduction and results in an increase in fuel consumption. Based on Oswatitsch criterion and aiming to maximize total pressure, Ran and Mavris (2005) defined an optimization methodology applied to supersonic inlet, considering atmospheric air as a calorically perfect gas and neglecting viscous effects. The methodology can be applied to a two-dimensional system with $(n-1)$ incident oblique shock system. According to Oswatitsch criterion, all incident shock waves have the same intensity, Eq. (9).

$$M_0 \cdot \sin(\beta_1) = M_{ic} \cdot \sin(\beta_{i+1}), \quad i = 1, 2, \dots, n - 2 \tag{9}$$

The methodology based on the modified optimization criterion of a 2D supersonic inlet to maximize total pressure, established by Ran and Mavris (2005), was first applied to 2D hypersonic inlet by Martos (2017). Considering a scramjet with $(n-1)$ ramps (Fig. 6), the deflection angles of the compression ramps are determined from the θ - β - M relationship of the oblique shock wave from the plane, considering atmospheric air as a calorically perfect gas and without viscous effects.

3.3 Expanding Section Design

The scramjet operates according to the open Brayton thermodynamic cycle (Fig. 2). In this case, the combustion products are released into the Earth’s atmosphere at the pressure corresponding to the flight altitude. Thus, regardless of the expansion section angle, it is possible to determine the scramjet’s trailing edge, where the pressure at the trailing edge is equivalent to the free stream pressure. As shown in Fig. 7, in the expansion section, the scramjet’s trailing edge must be coupled to the accelerator vehicle, which is responsible for bringing the scramjet to its operating conditions.

Without fuel injection, the air mass flow (\dot{m}) rate must be constant from the leading edge to the trailing edge of the scramjet (stations 0 to 10), Eq. (10).

$$\dot{m}_{air} = \rho_0 \cdot u_0 \cdot A_0 = \dots = \rho_{10} \cdot u_{10} \cdot A_{10} = \text{constant} \tag{10}$$

With fuel injection and assuming no heat loss to the walls, the total temperature, Eq. (11), and the air mass flow rate is constant until the combustion chamber entrance

Fig. 6 Optimization for maximum pressure recovery, adapted from Araújo et al. (2021)

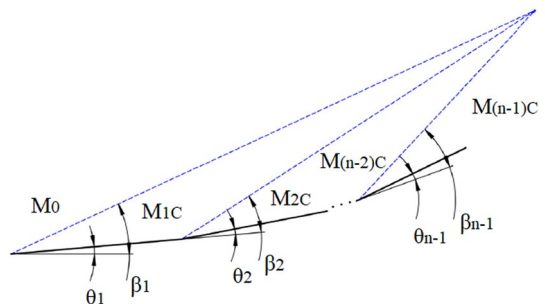
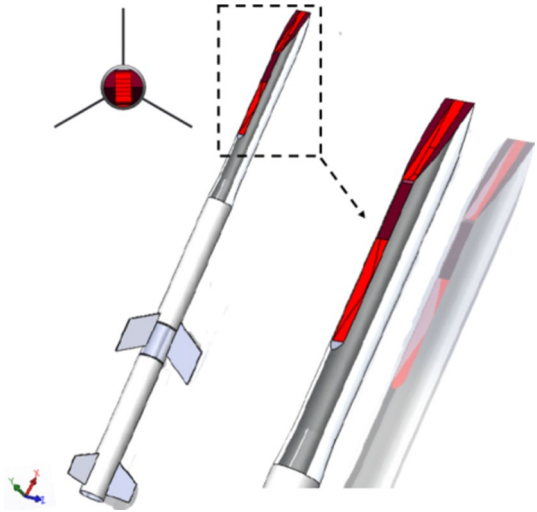


Fig. 7 Coupling the scramjet to the throttle vehicle (Carneiro et al. 2022)



(stations 0 to 3), Eq. (12). With the injection of fuel into the combustion chamber, the total temperature and the mass flow must be changed, remaining constant from the combustion chamber exit to the trailing edge of the scramjet (stations 4 to 10), Eq. (13).

$$T_{t_i} = \left(1 + \frac{\gamma - 1}{2} \cdot M_i^2 \right) \cdot T_i \quad (11)$$

$$\dot{m}_{inlet} = \rho_0 \cdot u_0 \cdot A_0 = \rho_3 \cdot u_3 \cdot A_3 \quad (12)$$

$$\dot{m}_{outlet} = \rho_4 \cdot u_4 \cdot A_4 = \rho_{10} \cdot u_{10} \cdot A_{10} \quad (13)$$

Assuming no combustion occurs from Stations 4 to 10, then the total temperature must remain constant from the combustor exit to the trailing edge. Thus, knowing the conditions at the combustion chamber exit, establishing that the pressure at the trailing edge (p_{10}) must be equal to the pressure (p_0) at flight condition, the Mach number at the trailing edge (M_{10}) can be determined, Eq. (14).

$$\frac{T_{t_{10}}}{T_{t_4}} = \frac{1 + \frac{\gamma-1}{2} \cdot M_{10}^2}{1 + \frac{\gamma-1}{2} \cdot M_4^2} \cdot \left(\frac{p_{10}}{p_4} \right)^{\frac{\gamma-1}{\gamma}} = 1 \quad (14)$$

3.4 Computational Model for Aerodynamic Analysis

The governing equations for compressible flow, in terms of the averages of the flow properties, known as Reynolds-Averaged Navier–Stokes equations (RANS) (Versteeg and Malalasekera 2007), consisting of continuity, momentum and energy equations, Eqs. (15) to (17) respectively, were solved using the Fluent module of the software Ansys (2021a).

$$\frac{\partial \bar{p}}{\partial t} + \frac{\partial}{\partial x_j} (\bar{\rho} \tilde{u}_j) = 0 \tag{15}$$

$$\frac{\partial}{\partial t} (\bar{\rho} \tilde{u}_i) + \frac{\partial}{\partial x_j} (\bar{\rho} \tilde{u}_i \tilde{u}_j + \delta_{ij} \bar{p}) = \frac{\partial}{\partial x_j} (\bar{\tau}_{ij} - \overline{\rho u_i'' u_j''}) \tag{16}$$

$$\frac{\partial}{\partial t} (\bar{\rho} \tilde{E}) + \frac{\partial}{\partial x_j} (\bar{\rho} \tilde{H} \tilde{u}_j) = \frac{\partial}{\partial x_j} (\bar{\tau}_{ij} \tilde{u}_i + \overline{\tau_{ij} u_i''} - \bar{q}_j - \overline{\rho H'' u_i''}) \tag{17}$$

For Newtonian fluids, the stress tensor is modeled according to the Stokes hypothesis, Eq. (18).

$$\bar{\tau}_{ij} \tag{18}$$

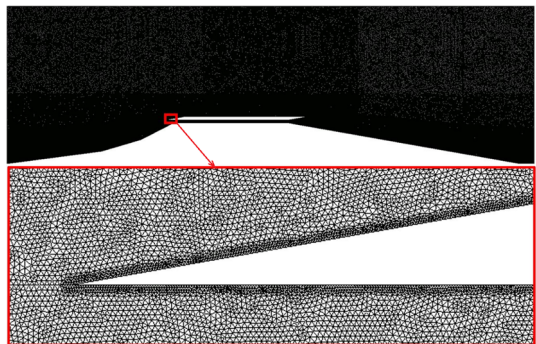
In the governing equations for compressible flow, terms with superscripted indices (\sim) have undergone density-weighted averaging or Favre averaging. Here, ρ represents density, u_i the velocity vector, δ_{ij} the Kronecker delta operator, p pressure, E total energy, H total enthalpy, τ_{ij} stress tensor, q_{ij} heat flux, and μ corresponds to the dynamic viscosity of the fluid. The terms in the form are referred to as Reynolds stresses, which are modeled through the Boussinesq hypothesis, Eq. (19).

$$\left(\overline{\rho u_i'' u_j''} \right) = \frac{2}{3} \left(\bar{\rho} \tilde{k} + \mu_t \frac{\partial \tilde{u}_k}{\partial x_k} \right) \delta_{ij} - \mu_t \left(\frac{\partial \tilde{u}_i}{\partial x_j} + \frac{\partial \tilde{u}_j}{\partial x_i} \right) \tag{19}$$

It was considered a density-based solver, an Implicit formulation with Roe-FDS flux type was considered. Least Squares Cell Based was employed for spatial discretization for the gradient, and Second Order Upwind for the flow.

In the analytical approach, the design of the expansion section aims to meet the Brayton thermodynamic cycle. In the numerical approach, the ramps of the expansion section extend until they intersect at the scramjet’s symmetry plane (Fig. 8), avoiding the formation of a recirculation zone and establishing a computational domain with the same characteristics for the cases without fuel injection (power-off) and with fuel combustion (power-on), allowing for comparison. In the computational domain (Fig. 8), an unstructured mesh with triangular elements was used, more suitable for numerical simulations applied to scramjets considering atmospheric air as a calorically perfect gas and without viscous effects. The

Fig. 8 Computational mesh of CFD analysis



validation of the CFD numerical results was developed based on the results of the theoretical-analytical analysis.

The input conditions of the computational domain refer to scramjet design flight conditions an altitude of 23 km and Mach number 5.8 (corresponding to flight speed of 1723 m/s).

The mesh convergence analysis was conducted using the Grid Convergence Index (GCI), as it consists of a more comprehensive analysis of model convergence, considering both the relative difference between two solutions and the mesh resolution and order of approximations, representing the measure of how far the obtained result is from the asymptotic numerical value (relative error limit) (Celik et al. 2008).

The mesh convergence analysis was evaluated for the temperature at the inlet of combustor, a condition required for spontaneous combustion of hydrogen fuel as per the optimization process carried out. For the finest mesh, an interior Grid Convergence Index (GCI) of less than 1% was observed (Table 3). The GCI ratio is approximately unitary, meaning the ratio between errors and mesh spacing remains nearly constant, meeting the asymptotic convergence range.

Note that with a finer mesh, the temperature value at the inlet of the combustion chamber is the one that gets closest to the required condition of 1071.25 K for burning the hydrogen-air mixture.

Following Rayleigh's theory, fuel combustion is modeled considering the addition of heat, but without the addition of fuel mass. In this case, we can apply in Fluent the heat added to the domain region representing the fuel injection, based on the energy equation, Eq. (17). Thus, the energy source term is applied based on Eq. (20), which indicates that the addition of heat alters the total energy. This simplification for the combustion chamber results in a more conservative approach.

$$\dot{q} = c_{p_{air}} \cdot (T_{t,4} - T_{t,3}) \quad (20)$$

3.5 Computational Model of Structural Analysis

The static structural analysis of the preliminary scramjet design was evaluated in the Static Structural module of the Ansys software. For a static structural analysis, the global displacement vector $\{x\}$ is determined by the matrix equation, Eq. (21), which is the matrix representation of the equilibrium equations in structural analyses, in which $[K]$ is the global stiffness matrix and $\{F\}$ is the global load vector (Ansys 2021b).

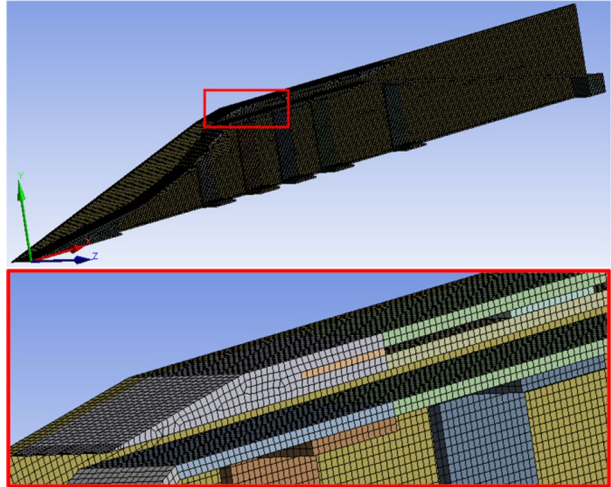
$$[K]\{x\} = \{F\} \quad (21)$$

To reduce the computational cost, it was decided to use a quarter of the scramjet geometry, since represents symmetries by the XY and XZ planes (Fig. 9). It is important to highlight that the structural model to be analyzed refers to the case with fuel combustion.

Table 3 Mesh information and GCI indexes

	Coarse (1)	Fine (2)	Dense (3)
N. of elements	1,936,244	3,725,810	7,209,893
T (K)	1079.42	1075.11	1072.16
GCI_{21}	1.09%	GCI_{32}	0.75%

Fig. 9 Computational mesh of structural analysis



When configuring the software to generate the mesh over the structural domain, the Automatic Method option was selected (Fig. 9). Based on a previous convergence analysis, a mesh with an average element size of 3.5 mm was established (132,168 elements and 705,360 nodes). The generated mesh was formed predominantly by hexahedral elements, but due to the wedges, the discretization also presented tetrahedral elements. The hexahedral elements were of the SOLID186 type and had 20 nodes, whereas the tetrahedral elements were of the SOLID187 type and had 10 nodes, but both with three degrees of freedom per node in the x, y and z directions.

In contact surface conditions, to simulate the non-linearity of contact between the elements of the structure, bonded contact was applied, which characterizes that the parts have interaction, but there was no separation or displacement between them. Also, as the model considered a quarter of the geometry, it was established that faces cut in the XY plane have no z-displacement, faces cut in the XZ plane have no y-displacement, and in the coupling region in the expansion section, there was no x-displacement.

In the scramjet, the leading edges of the vehicle and the fairing, as well as the surfaces at the entrance of the combustion chamber were made of Inconel 718. In the internal structure, formed by the stringers and ribs, the material used was Stainless Steel 304. In the other structures of the scramjet (ramps and side panel) Aluminum 7075 was used (Fig. 10). In complementary analyzes other materials were used, Tungsten was considered to replace Inconel 718 (Fig. 11).

Basically, the definition of materials must take into account mechanical capacity, weight and availability. Table 4 shows the mechanical properties of the materials used, incorporated into the Engineering Data of the Static Structural module: density (ρ), modulus of elasticity (E), Poisson's ratio (ν), tensile yield strength (σ_y) and tensile ultimate strength (σ_{ut}).

Materials for the engineered scramjet were chosen according to the specifications outlined for the X-51A. This hypersonic vehicle predominantly utilizes traditional metals for its fundamental structure. Specifically, the internal airframe and bulkheads are fashioned from machined aluminum. To endure the intense heat experienced at the nose tip and provide stability along its longitudinal axis, a tungsten nose cap is utilized. This component is further fortified with a thermal barrier coating of silicon dioxide. Positioned atop an

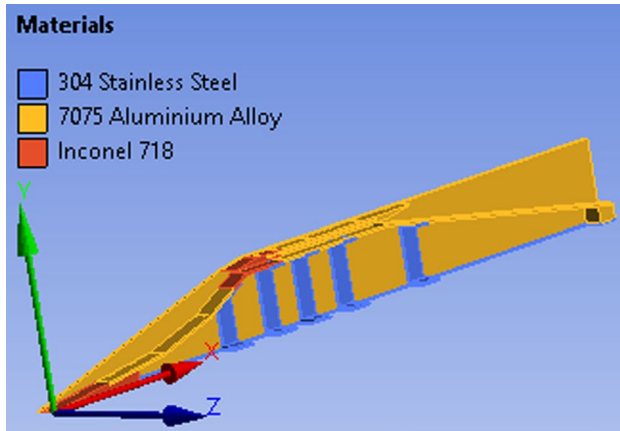


Fig. 10 Specifications of the materials used in the scramjet structure

Fig. 11 Replacement of Inconel 718 with Tungsten in the scramjet

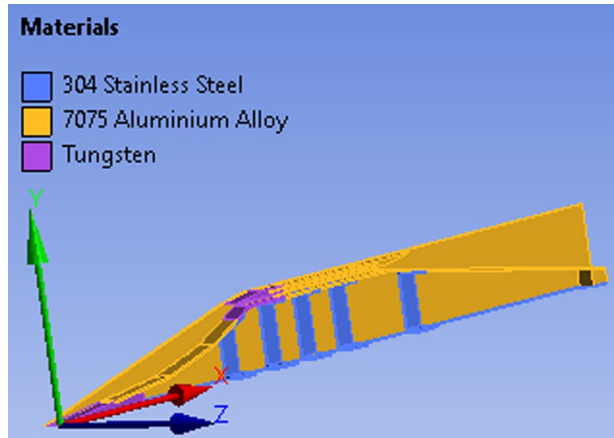


Table 4 Mechanical properties of the materials used, adapted from MATWEB (2022)

Material	ρ (g/cm ³)	E (GPa)	ν	σ_y (MPa)	σ_{ut} (MPa)
Stainless steel 304	8	200	0.29	215	505
Aluminum 7075	2.81	71.7	0.33	503	572
Inconel 718	8.19	204.9	0.284	980	1100
Tungsten	19.25	411	0.26	750	980

Inconel nose cap adapter, it effectively prevents thermal conduction to the remainder of the vehicle (Hank et al. 2008).

Similar materials were also employed in the aero-thermo-structural analysis of scramjet within the scope of the Mach 8 SCRAMSPACE flight-test engine, constructed from common engineering materials. These include a 5 mm thick aluminum fairing,

aluminum inlet and combustion chamber with 8–10 mm thickness, and a thrust nozzle composed of carbon-phenolic material with a thickness ranging from 4 to 8 mm (Capra et al. 2015, 2018).

The boundary conditions applied to the scramjet structure refer to the aerodynamic pressure load, defined from the analytical analysis considering the theories that described the flow behavior along the streamline from the leading edge to the trailing edge of the scramjet (Fig. 3), and validated from the CFD. The weight force of the structure and the acceleration of $78,480 \text{ mm/s}^2$ provided by the S30 and S31 rocket engines were considered.

Initially, 6 mm thick sheets were considered throughout the scramjet generic structure design (thicknesses also based on the specifications for X-51A and SCRAMSPACE). In complementary analyses, the behavior of the structure was evaluated by reducing the thickness of the plates, so that cases with 4 mm, 3 mm and 2.5 mm were considered.

4 Results and Discussions

For calorically perfect gas, the required temperature of air at the combustion chamber entrance for auto-ignition of hydrogen fuel was 1071.25 K, constant for any Mach number and flight altitude, depending only on the specific heat at constant pressure of atmospheric air and on parameters related to the fuel, considering stoichiometric burn.

The temperature of 1071.25 K was high enough to transfer energy to increase the hydrogen injection temperature, estimated at 300 K, to the auto-ignition temperature of 845.15 K, allowing spontaneous combustion of the hydrogen injected in the combustion chamber.

For the temperature of 1071.25 K the Mach number required at the combustion chamber entrance was 1.71 (supersonic flow), considering scramjet flying at an altitude of 23 km and speed of 1723 m/s, corresponding to Mach number 5.8.

The compression section optimization criterion (Table 5) considers that all incident oblique shock waves have the same intensity (the normal components $M_{in, sen}(\beta)$ remains constant) and that the conditions required at the combustion chamber entrance (temperature T_3 and Mach number M_3) must be satisfied, ensuring spontaneous combustion at supersonic speed.

The efficiency of the inlet was higher as the number of ramps increases from 1 to 5 (Table 5) and the increase in the total pressure ratio (π) in the external compression section (through the incident shock waves) was verified, resulting in minimum losses of total pressure, reduction of the thermodynamic properties ratios. The increase in the number of ramps was accompanied by a reduction in the total pressure ratio (through the reflected shock wave), resulting in less static entropy variation at the combustion chamber entrance. As expected, the required conditions of temperature T_3 and Mach number M_3 were satisfied.

Although efficiency increased as more compression ramps were considered, efficiency gains were reduced in models with a higher number of ramps. When analyzing the percentage change (i), Eq. (22), between the values (v) of the total pressure ratio between stations 3 and 0 (p_{t3}/p_{t0}), a scramjet with two ramps is 80% more efficient than one with just one ramp. Furthermore, a scramjet with five ramps exhibits a 13.64% efficiency advantage over a three-ramp scramjet, and only a 4.17% increase in efficiency compared to a four-ramp scramjet.

Table 5 Optimization of the scramjet compression section in the flight condition at an altitude of 23 km and Mach number 5.8

	1 ramp	2 ramps	3 ramps	4 ramps	5 ramps
<i>External compression section (incident shock waves)</i>					
θ_1 (°)	23.96	11.36	7.48	5.57	4.43
β_1 (°)	33.23	19.20	15.58	13.95	13.04
M_{1C}	2.89	4.35	4.84	5.08	5.23
θ_2 (°)	–	15.08	8.93	6.34	4.91
β_2 (°)	–	26.00	18.77	15.97	14.50
M_{2C}	–	3.14	3.99	4.43	4.69
θ_3 (°)	–	–	10.77	7.25	5.45
β_3 (°)	–	–	22.98	18.42	16.20
M_{3C}	–	–	3.22	3.82	4.19
θ_4 (°)	–	–	–	8.34	6.07
β_4 (°)	–	–	–	21.45	18.19
M_{4C}	–	–	–	3.26	3.72
θ_5 (°)	–	–	–	–	6.79
β_5 (°)	–	–	–	–	20.57
M_{5C}	–	–	–	–	3.28
$M_{in} \text{ sen}(\beta)$	3.18	1.91	1.56	1.40	1.31
P_{out}/P_{in}	11.62	4.08	2.66	2.11	1.83
T_{out}/T_{in}	2.90	1.61	1.36	1.25	1.20
π	0.28	0.76	0.91	0.96	0.98
<i>Internal compression section (reflected shock wave)</i>					
θ_{ref} (°)	23.96	26.43	27.19	27.50	27.66
β_{ref} (°)	43.73	45.02	45.42	45.59	45.68
M_3	1.71	1.71	1.71	1.71	1.71
T_3 (K)	1071.25	1071.25	1071.25	1071.25	1071.25
p_3 (Pa)	180,734.76	321,589.51	392,506.44	427,818.70	446,983.15
π	0.72	0.62	0.58	0.57	0.56
p_{i3}/p_{i0}	0.20	0.36	0.44	0.48	0.50

$$i = \frac{v_{new} - v_{initial}}{v_{initial}} \cdot 100 \quad (22)$$

Evidently, considering models with more ramps where the incident shock waves must intersect at specific deflection angles makes the execution more expensive. The manufacturing difficulty coupled with less significant gains in efficiency makes the scramjet with three compression ramps the ideal optimization condition.

A scramjet, with three compression ramps at angles of 7.48°, 8.93° and 10.77° flying at an altitude of 23 km at a speed corresponding to Mach number 5.8 was capable of generating at the combustion chamber entrance temperature of 1071.25 K and Mach number 1.71 (Tables 5, 6), sufficient for supersonic combustion of hydrogen.

Considering a scramjet compression section with three ramps, the normal components $M_{in} \text{ sen}(\beta)$ remained constant for all ramps (Table 6), due to the optimization criterion that considers that all incident shock waves had the same intensity, also keeping

Table 6 Thermodynamic properties of the flow in the compression section of the scramjet

	Station 0	Ramp 1	Ramp 2	Ramp 3	Reflection	Entrance
M_{in}	5.8	5.8	4.84	3.99	3.22	1.71
θ (°)	–	7.48	8.93	10.77	27.19	–
β (°)	–	15.58	18.77	22.98	45.42	–
$M_{in} \sin(\beta)$	–	1.56	1.56	1.56	2.30	–
M_{out}	–	4.84	3.99	3.22	1.71	–
p_{out}/p_{in}	–	2.66	2.66	2.66	5.99	–
T_{out}/T_{in}	–	1.36	1.36	1.36	1.944	–
ρ_{out}/ρ_{in}	–	1.96	1.96	1.960	3.081	–
π	–	0.91	0.91	0.91	0.585	–
p (Pa)	3466.86	9235.67	24,603.71	65,544.00	392,506.44	392,506.44
T (K)	219.57	298.39	405.50	551.07	1071.25	1071.25
ρ (kg/m ³)	0.05501	0.10783	0.21137	0.41435	1.27641	1.27641
a (m/s)	297.05	346.29	403.68	470.59	656.13	656.13
u (m/s)	1723	1676.41	1610.94	1517.44	1121.33	1121.33
T_i (K)	1697.01	1697.01	1697.01	1697.01	1697.01	1697.01
\dot{m} (kg/s)	18.01	–	–	–	–	18.01

constant the thermodynamic properties ratios and the total pressure ratio in the external compression section. Through each oblique shock wave (incident and reflected) the air flow was compressed and decelerated, increasing the value of the thermodynamic properties (pressure, temperature, density and sound speed), reducing the flow velocity and the Mach number (remaining supersonic) (Table 6). Furthermore, the total temperature remained constant as per the law of conservation of energy.

In the combustion chamber, without fuel injection (Table 7), the thermodynamic air properties and Mach number values at the entrance and exit were the same. Consequently, the thermodynamic property ratios at the exit were unity and the values of the thermodynamic properties (pressure, temperature, density and sound speed), as well as the airflow velocity, remained constant inside the combustion chamber.

In the expansion section the gases expanded to a pressure of 3466.86 Pa at the trailing edge, equivalent to the freestream pressure at flight condition of an altitude of 23 km (Table 7). The reduction in the values of the thermodynamic properties in the expansion were accompanied by an increase in the flow velocity to 1688.96 m/s, less than 1723 m/s, demonstrating that without energy addition the scramjet cannot generate thrust. As there was no energy increment to the flow, the total temperature remained constant from the leading edge to the trailing edge of the scramjet.

In the expansion section the scramjet must be coupled to the accelerator vehicle. For coupling it is necessary to truncate the expansion ramp, so that the trailing edge is not sharp (with ramps intersecting on the symmetry axis that passes from the leading edge to the trailing edge). Thus, the expansion section optimization checks the point on the ramp where the pressure condition is equivalent to that of free flow ($p_0 = p_{10}$), where the truncation is performed. A pressure of 3466.86 Pa is reached for a flow with a velocity corresponding to Mach 5.06 at the trailing edge. For this Mach number the height of the expansion plume is 244.86 mm. Assuming that the expansion occurs at an angle of 10°

Table 7 Thermodynamic properties of the airflow in the combustion chamber and expansion sections of the scramjet (power-off)

	Entrance	Exit	Prandtl–Meyer	Station 10
M_{in}	1.71	1.71	1.71	2.06
θ (°)	–	10	–	–
v (M_{in}) (°)	–	–	18.07	–
v (M_{out}) (°)	–	–	28.07	–
M_{out}	–	1.71	2.06	5.06
p_{out}/p_{in}	–	1	0.58	0.02
T_{out}/T_{in}	–	1	0.86	0.30
ρ_{out}/ρ_{in}	–	1	0.68	0.05
p (Pa)	392,506.44	392,506.44	227,884.04	3466.86
T (K)	1071.25	1071.25	917.12	277.37
ρ (kg/m ³)	1.27641	1.27641	0.86562	0.04354
a (m/s)	656.13	656.13	607.10	333.87
u (m/s)	1121.33	1121.33	1251.83	1688.96
T_t (K)	1697.01	1697.01	1697.01	1697.01
\dot{m} (kg/s)	18.01	18.01	–	18.01

the length of the ramp is 658.65 mm (power-off). Under these conditions, the scramjet geometry is defined for the case no fuel burning.

Considering hydrogen-air burning (power-on) (Table 8) the Mach number at the combustion chamber exit must be $M_4 \geq 1.1$ so that the added heat from fuel combustion did not slow down the combustion products to subsonic condition. Simulating combustion of hydrogen-air mixture in supersonic velocity the heat addition of Rayleigh theory with constant area and no fuel mass added, the values of the thermodynamic properties increased, and the flow velocity was reduced at the combustion chamber exit, but the combustion product velocity remained supersonics.

Table 8 Thermodynamic properties of the flow in the combustion chamber and expansion section of the scramjet (power-on)

	Entrance	Exit	Prandtl–Meyer	Station 10
M_{in}	1.71	1.71	1.1	1.48
θ (°)	–	10	–	–
v (M_{in}) (°)	–	–	1.34	–
v (M_{out}) (°)	–	–	11.34	–
M_{out}	–	1.1	1.48	4.87
p_{out}/p_{in}	–	1.89	0.60	0.01
T_{out}/T_{in}	–	1.48	0.86	0.25
ρ_{out}/ρ_{in}	–	1.28	0.69	0.03
p (Pa)	392,506.44	741,438.23	443,454.93	3466.86
T (K)	1071.25	1583.63	1367.34	341.90
ρ (kg/m ³)	1.27641	1.63102	1.12983	0.03532
a (m/s)	656.13	797.76	741.28	370.68
u (m/s)	1121.33	877.54	1097.58	1806.98
T_t (K)	1697.01	1966.87	1966.87	1966.87
\dot{m} (kg/s)	18.01	18.01	–	18.01

Also, burning fuel increased the total energy, raising the total temperature from 1697.01 to 1966.87 K. Again, in the expansion section, the gases expanded to a pressure of 3466.86 Pa at the trailing edge (Table 8), but with power-on the flow velocity was 1806.98 m/s (station 10), higher than at 1723 m/s, demonstrating the capability to generate thrust when fuel was burned.

The Mach number of the flow that establishes a pressure of 3466.86 Pa at the trailing edge of the scramjet considering the power-on approach is 4.87. Thus, for the same value of trailing edge pressure, the Mach number with power-on is lower compared to the case with power-off, since burning fuel reduces the Mach number of the combustion chamber output. The height of the expansion plume is 282.11 mm (greater than for power-off) and the length considering an expansion with a 10° angle of the expansion ramp is 764.29 mm (power-on), that is, with burning of fuel the gases released from the combustion chamber must be expanded further until reaching the free-flow pressure condition at an altitude of 23 km.

The Mach number of the flow that establishes a pressure of 3466.86 Pa at the trailing edge of the scramjet considering the power-on approach is 4.87. Thus, for the same value of trailing edge pressure, the Mach number with power-on is lower compared to the case with power-off, since burning fuel reduces the Mach number of the combustion chamber output. The height of the expansion plume is 282.11 mm (greater than for power-off) and the length considering an expansion with a 10° angle of the expansion ramp is 764.29 mm (power-on), that is, with burning of fuel the gases released from the combustion chamber must be expanded further until reaching the free-flow pressure condition at an altitude of 23 km.

Under these conditions, the preliminary geometry of the scramjet is established (Fig. 12). The geometry must correspond to the case with fuel combustion, but the conditions at the trailing edge are also evaluated using CFD in both approaches.

In the contours (Fig. 13), the disturbances in the flow become more evident as the value variations are more representative. Considering no fuel injection the pressure contours (Fig. 13a) the first shock wave is imperceptible, since the pressure in the first ramp represents only 2.37% of the variation of the value until the combustion chamber, while in the third ramp it represents 16.85% (Eq. 22). Still, analyzing the density contour (Fig. 13b), for example, the value in the first ramp corresponds to 8.83% of the variation and for this reason the first shock wave is perceptible. The temperature (Fig. 13c) and sound speed (Fig. 13d) contours are simulated, as temperature is the only variable used to determine the sound velocity. As expected, the compression section acts by reducing the flow velocity (Fig. 13e) up to the combustion chamber entrance. Numerical simulation allowed to verify that the scramjet design was capable of meeting the conditions of shock on-lip and shock on-corner (Fig. 13f), guaranteeing maximum capture of

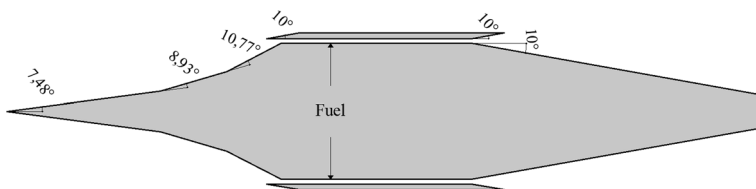


Fig. 12 Hydrogen-air burning (power-on) at the scramjet combustion chamber in flight condition of 23 km and Mach number 5.8

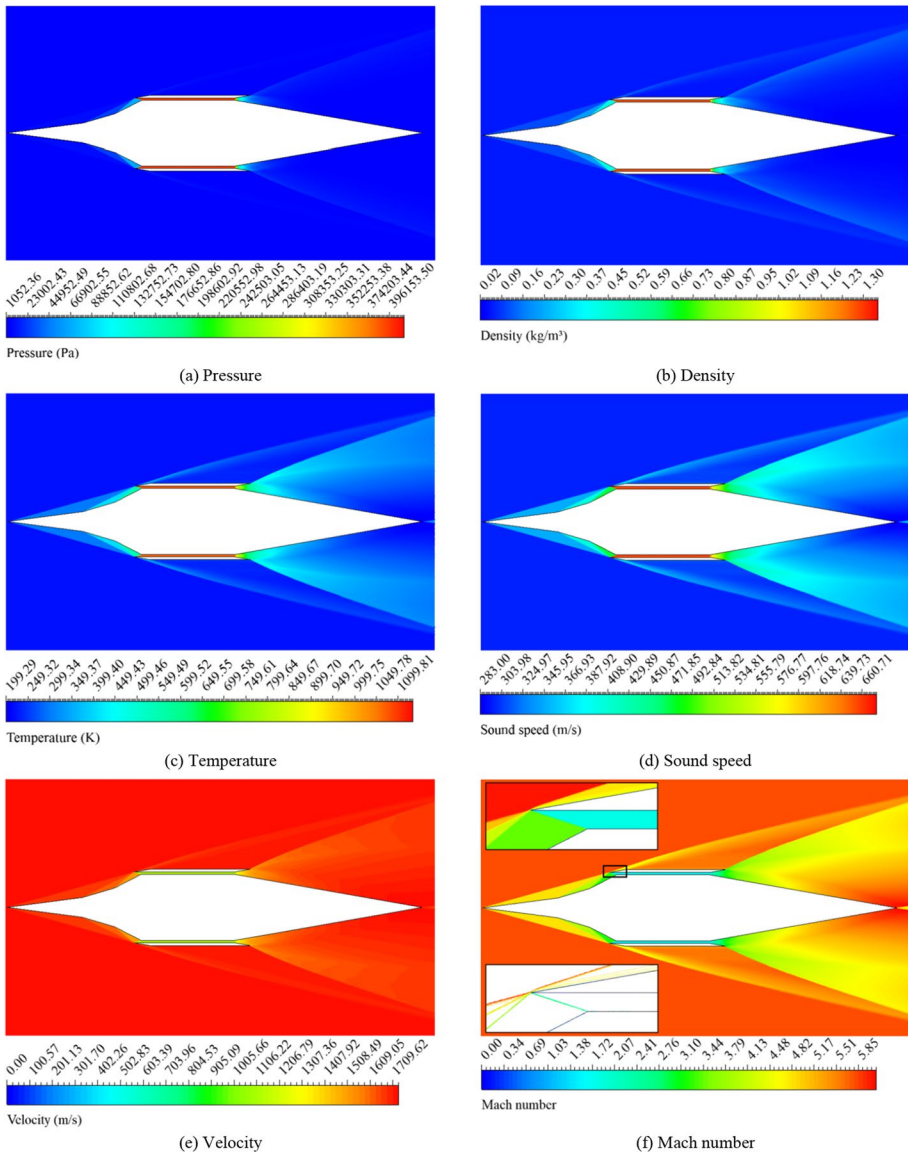


Fig. 13 Contours of thermodynamic properties, flow velocity and Mach number in scramjet (power-off)

atmospheric air by the compression section, characterized by a mass flow of 17.94 kg/s at the combustion chamber entrance, and no shock train formation.

Considering no hydrogen injection the numerical results show good agreement with the analytical results (Fig. 14) and the behavior of thermodynamic properties, pressure (Fig. 14a), density (Fig. 14b), temperature (Fig. 14c) and sound speed (Fig. 14d), as well as the flow velocity (Fig. 14e) and Mach number (Fig. 14f) along the surface streamline of the scramjet was adequately represented by the numerical simulation. Regarding the

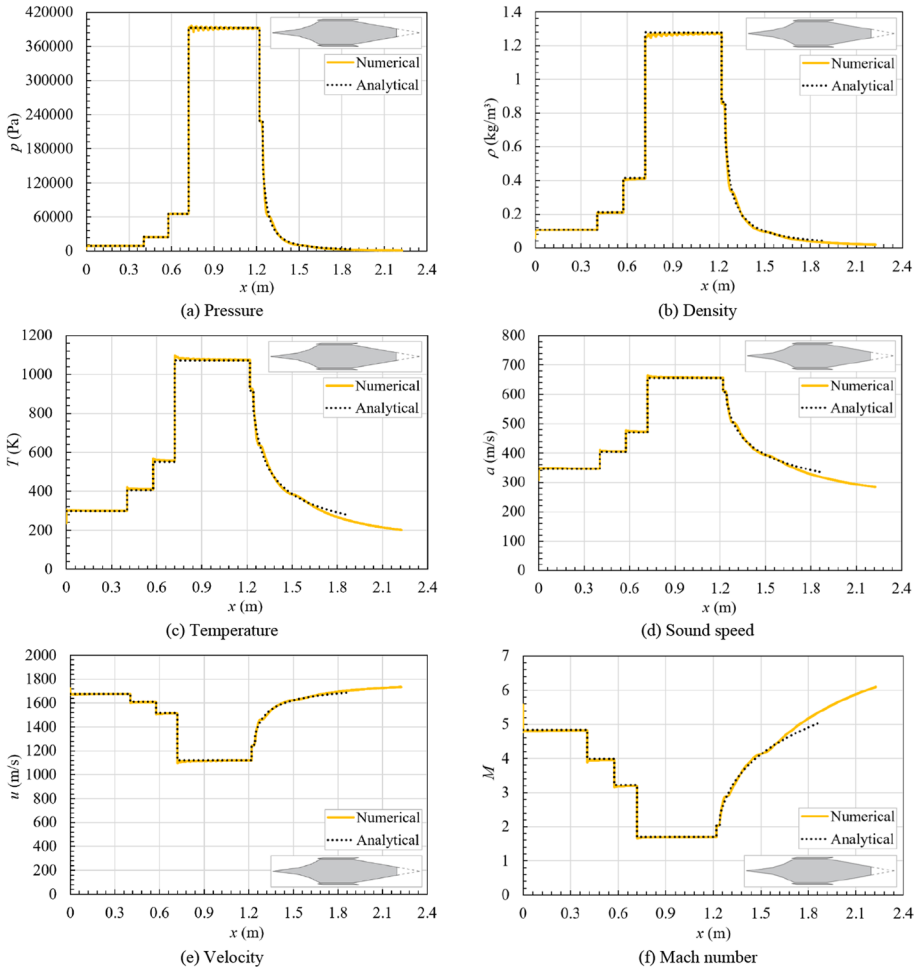


Fig. 14 Comparison between analytical and numerical results regarding the behavior of thermodynamic properties, flow velocity and Mach number along the streamline on the surface of the scramjet in the condition no hydrogen injection (power-off)

conditions required in the combustion chamber for the auto-ignition of hydrogen fuel, compared to the analytical results, at the end of the isolator the temperature varied by 0.65% and the Mach number by 1.17% (Eq. 22). For the numerical result, the gases released from the combustion chamber expanded further to the respective trailing edge, since truncation of the numerical model was not considered to avoid the formation of a recirculation zone.

With a mass flow of 17.94 kg/s and a combustion chamber height of 12.58 mm, the amount of energy that must be added to the flow, in a region with a length of 1 mm at the beginning of the combustor (Fig. 1), to simulate the burning of fuel was of 386.74 GW/m³, sufficient for stoichiometric burning ($\phi = 1$) of the fuel with atmospheric air captured by the compression section, maintaining supersonic flow at the exit of the combustion chamber ($M = 1.1$). With fuel burning, the value of thermodynamic properties, pressure (Fig. 15a), density (Fig. 15b), temperature (Fig. 15c) and sound speed (Fig. 15d), were higher in the

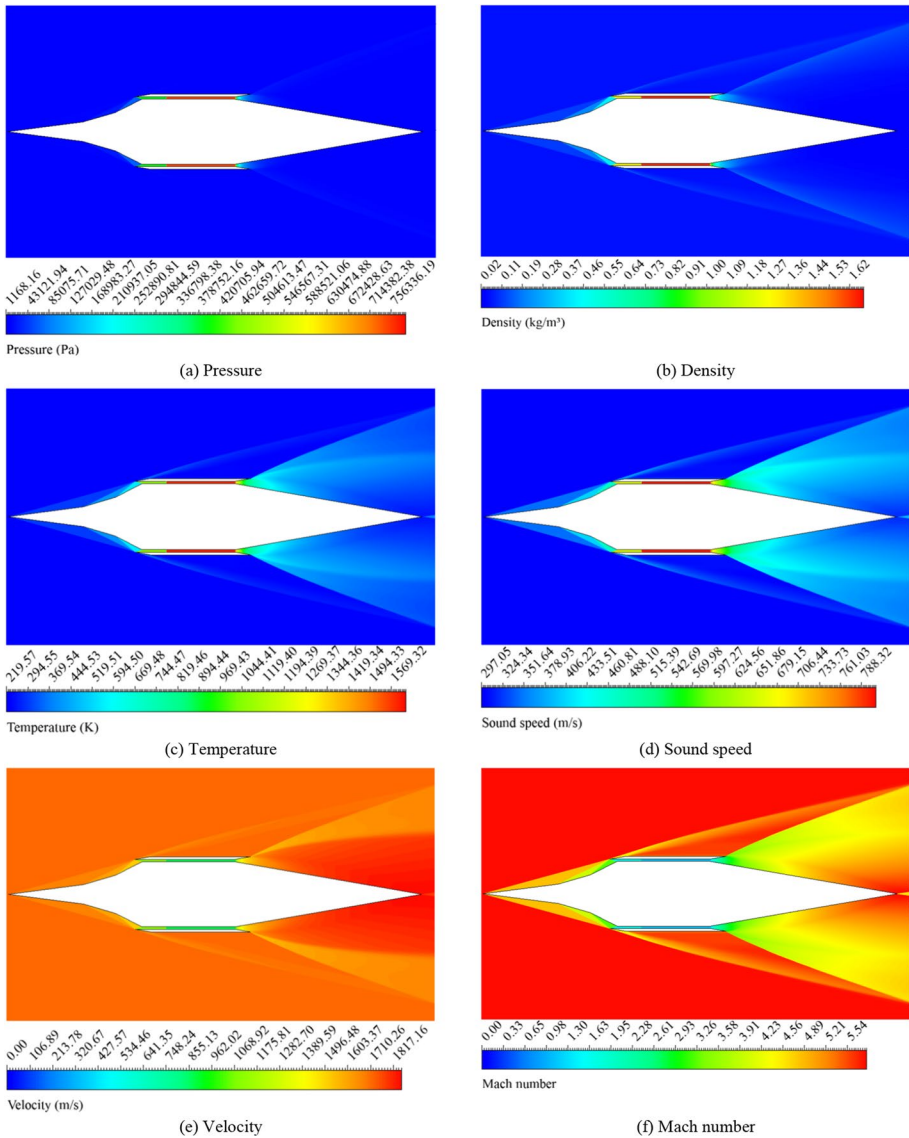


Fig. 15 Contours of thermodynamic properties, flow velocity and Mach number in scramjet (power-on)

combustor of the scramjet combustion chamber, while the flow velocity (Fig. 15e) and Mach number (Fig. 15f) were lower. With the greater variation of the conditions in the combustion chamber, the pressure in the first and second ramps represented, respectively, only 1.25% and 3.33% of the variation of the pressure value of the freestream atmospheric airflow condition at 23 km to the burn fuel.

The contour lines for pressure in the combustor are verified in Fig. 16, considering hydrogen fuel combustion, simulated by applying the heat released from fuel combustion, according to Rayleigh’s theory, as a source term to the domain.

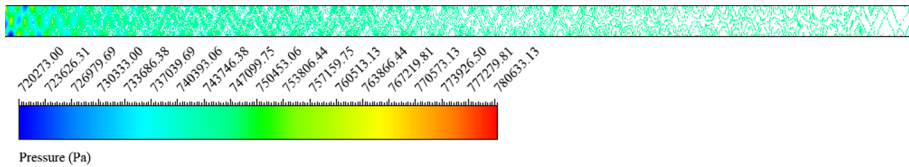


Fig. 16 Pressure contour lines in the scramjet combustor considering Rayleigh heat addition to simulate fuel burning (power-on)

With fuel combustion the numerical results also have good agreement with the analytical results. Evidently, from the leading edge to the end of the isolator, the value of thermodynamic properties, pressure (Fig. 17a), density (Fig. 17b), temperature (Fig. 17c) and sound speed (Fig. 17d), as well as the flow velocity (Fig. 17e) and the Mach number (Fig. 17f), was the same for the cases no burning fuel (power-off) and fuel-burning (power-on).

As in the numerical model, the expansion ramps intersect at the scramjet's axis of symmetry, and the dimensions are the same for both the power-off and power-on cases. Due to the heat addition from fuel combustion, the pressure at the trailing edge of the numerical model (station 10) is 1191.67 Pa, higher than the pressure of 1086.42 Pa in the case without fuel combustion. These pressure values are slightly lower than the freestream pressure at an altitude of 23 km, evaluated at 3466.86 Pa.

Although the design of the expansion section aims to meet the Brayton thermodynamic cycle, note in Figs. 14 and 17 that the conditions at the scramjet's trailing edge are slightly different. This discrepancy between numerical and analytical results is likely due to the presence of shock waves at the combustion chamber exit, a phenomenon not captured by the analytical analysis.

Evidently, there is an increase in the value of the equivalent von Mises stress in the scramjet structure according to the thickness of the plate (Figs. 18, 19). Considering a sheet with a thickness of 6 mm, the von Mises equivalent stress is verified at the leading edge of the fairing (Figs. 18a, 19a), close to the contact with the side panel, due to the small contact area, as well as the high static pressure values, referring to the conditions after the reflected shock wave. Note that with 6 mm sheet, there is a greater difference in the maximum von Mises equivalent stress value with the replacement of Inconel 718 by Tungsten, as the material change occurred mainly for the leading edges. For cases with sheets with a thickness of 4 mm (Figs. 18b, 19b) the gains in von Mises equivalent stress are not significant, but with the reduction of the thickness the maximum value starts to be verified in the combustor, region in which the static pressure value is also maximum with the burning of fuel. In this case, as different materials were not considered inside the combustion chamber (Aluminum 7075 was kept), there is little variation in the maximum von Mises equivalent stress results for the same sheet thickness (4 mm, 3 mm and 2.5 mm).

Note that for cases with 6 mm and 4 mm thick sheets, the von Mises equivalent stress value is lower than the yield stress of the materials used (215 MPa for Stainless Steel 304, 503 MPa for Aluminum 7075, 980 MPa for Inconel 718 and 750 MPa for Tungsten), that is, it does not exceed the elastic limit nor the yield point. Working in an elastic regime, the stresses are directly proportional to the strains. Furthermore, as it occurs in the elastic regime, the maximum strain in the structure is not permanent, being recoverable if the loads are removed, desirable for structures that will be used more than once.

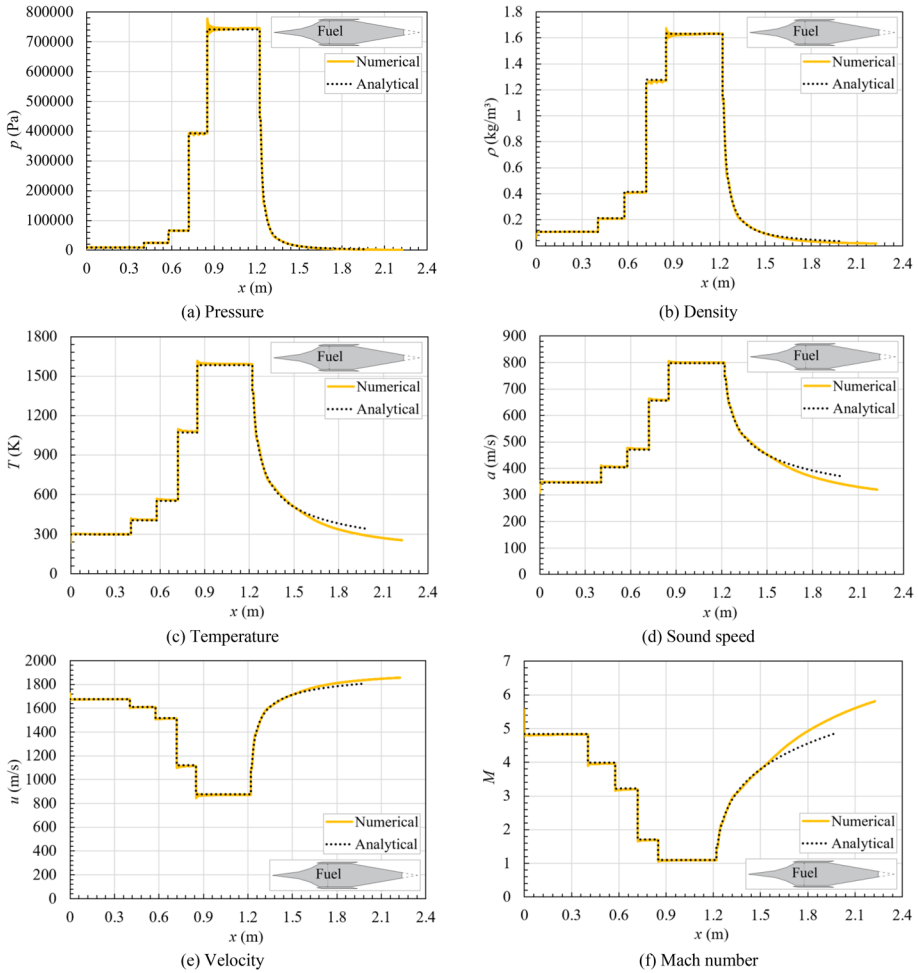


Fig. 17 Comparison between analytical and numerical results regarding the behavior of thermodynamic properties, flow velocity and Mach number along the streamline on the scramjet surface in the fuel-burning condition (power-on)

Although with a 3 mm plate (Figs. 18c, 19c) the value of 306.9 MPa is higher than the yield strength of Stainless Steel 304, only the internal structure (spars and ribs) is made of this material. In this case, in the stringers, the von Mises equivalent stress levels are less than 200 MPa. Only with 2.5 mm sheets (Figs. 18d, 19d) is the stringers yielding verified, resulting in plastic/permanent strains.

Regarding the materials used, changing Inconel 718 by Tungsten on the vehicle's leading edges and fairing, as well as on the combustion chamber inlet surface, results in little change in the mechanical capacity of the model and considerable increase in weight, which is not desirable. In Fig. 20, the mass of the complete scramjet model is verified for the different cases considered. Basically, there is a difference of 17–18 kg between models with Inconel 718 (lighter) and Tungsten.

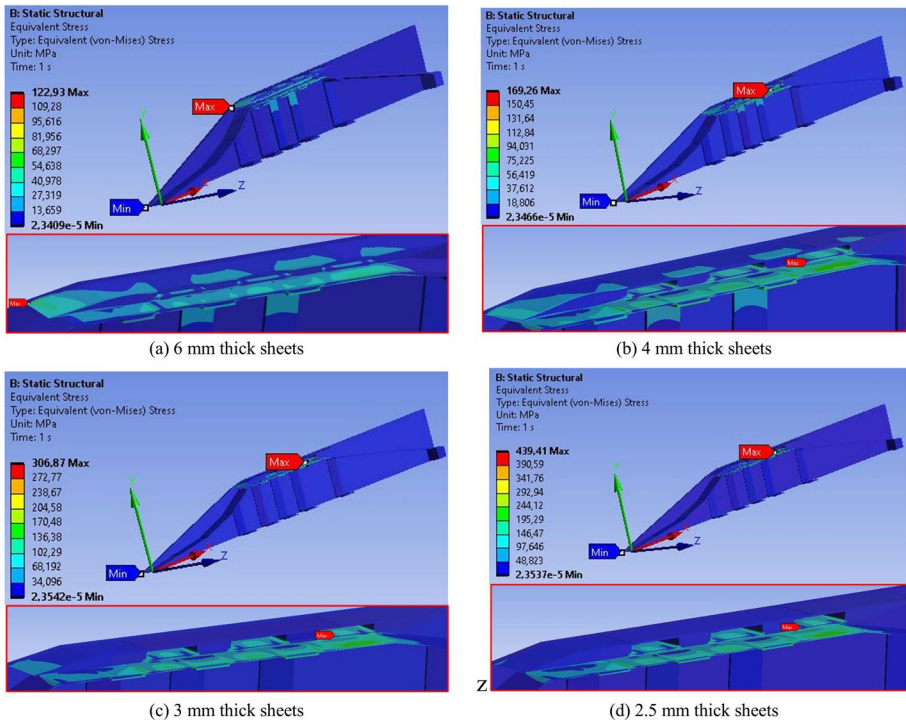


Fig. 18 Equivalent von Mises stress in the scramjet structure designed considering Inconel 718 at the leading edges

5 Conclusions

Considering the criterion of maximum air capture and incident shock waves of the same intensity, the compression section of the supersonic combustion demonstrator with three ramps constitutes the ideal optimization condition to increase the vehicle compression efficiency and minimize the effects of entropy generation. At the entrance to the combustion chamber, without making manufacturing expensive.

A scramjet with compression ramps with deflection angles of 7.48° , 8.93° and 10.77° under flight conditions at an altitude of 23 km and a speed corresponding to Mach 5.8 is capable of providing, in the combustion chamber inlet, Mach number of 1.709 and temperature of 1071.25 K (greater than 845.15 K), sufficient for supersonic combustion of hydrogen fuel. In the aerodynamic analysis of the scramjet, the numerical results show good agreement with the analytical results.

The unstructured mesh with triangular elements proved to be more suitable to capture the flow conditions after the oblique shock waves, formed in the compression section of the scramjet. Also, the numerical simulations made it possible to verify that the on-lip and on-corner shock conditions are duly met for the projected model, without the formation of a shock train in the combustion chamber. In this sense, the analytical approach consists of a simple and fast alternative to provide the value of thermodynamic properties (pressure, density, temperature and sound speed), flow velocity and Mach number along the streamline from the leading edge to the trailing edge of the scramjet.

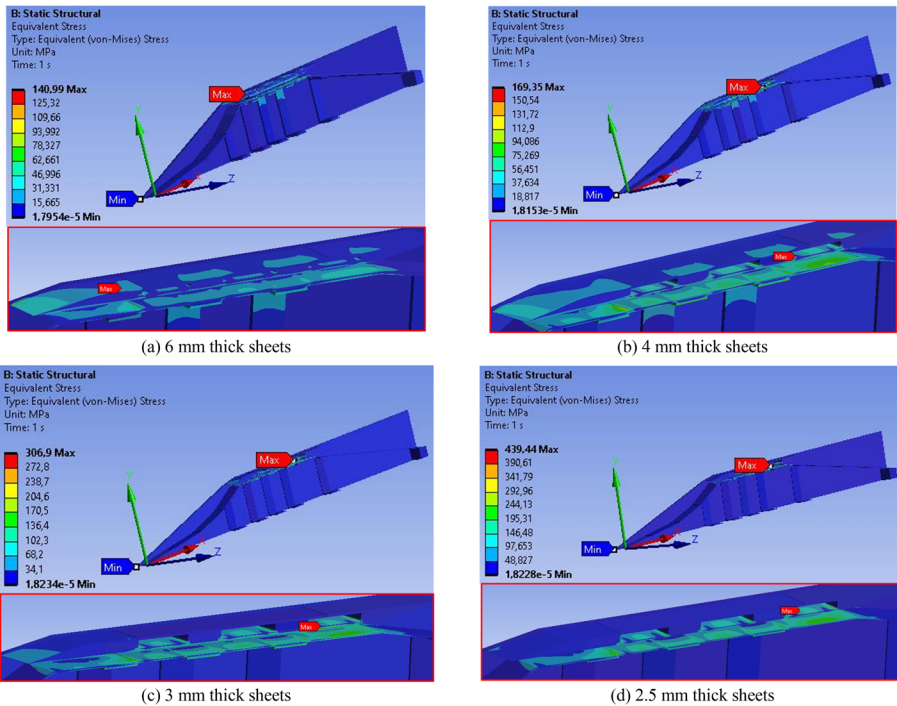
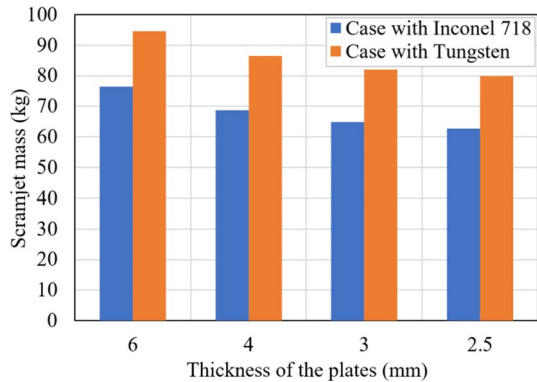


Fig. 19 Equivalent von Mises stress in the scramjet structure designed considering Tungsten at the leading edges

Fig. 20 Scramjet mass for different sheet thicknesses



In the structural analysis by numerical simulation, it was found that the maximum value of von Mises equivalent stress is lower than the yield stress of the materials considered (Stainless Steel 304, Aluminum 7075, Inconel 718 and Tungsten) for cases with 3 mm or higher. Under these conditions, the structure works in an elastic regime, so that the strains are recoverable. Only with 2.5 mm plates, there is flow of the internal structure spars, precisely in the combustion chamber, a region in which the structure is most requested by the aerodynamic pressure loads resulting from the flight at an altitude of 23 km with a speed

corresponding to the number of Mach 5.8. In addition, Inconel 718 is more suitable than Tungsten for application on the leading edges of the demonstrator, providing good mechanical capacity with low weight, being more advantageous for the scramjet.

Acknowledgements This study was financed in part by the Coordenação de Aperfeiçoamento de Pessoal de Nível Superior—Brasil (CAPES)—Finance Code 001. This work was carried out with the support of the Academic Cooperation Program in National Defense (PROCAD-DEFESA), Grant 88881.387753/2019-01, and the Aero-Thermo-Structural Project of Supersonic Combustion Demonstrator, Grant 405558/2022-8. The first author is funded by CAPES, Grant 88887.830228/2023-00. The third author is funded by Conselho Nacional de Desenvolvimento Científico e Tecnológico (CNPq), Grant 306004/2020-8. The authors would like to thank the Instituto Tecnológico de Aeronáutica (ITA) and the Universidade Federal do Rio Grande do Norte (UFRN) to support granted to carry out research on hypersonic airbreathing propulsion.

Author Contributions All authors contributed to the study conception and design.

Funding The authors declare they have no financial interests.

Data Availability Data are available upon request.

Declarations

Competing interests The authors declare no competing interests.

Conflict of interest The authors declare that they have no conflict of interest.

References

- Anderson, J.D., Jr.: *Modern Compressible Flow: with Historical Perspective*. McGraw-Hill series in Aeronautical and Aerospace Engineering, Boston (2003)
- ANSYS, Inc.: *Ansys fluent theory guide*. Canonsburg, PA: Release 2021 R2, 15317 (2021a)
- ANSYS, Inc.: *Ansys mechanical theory guide*. Canonsburg, PA: Release 2021 R2, 15317 (2021b)
- Araújo, P.P.B., Pereira, M.V.S., Marinho, G.S., Martos, J.F.A., Toro, P.G.P.: Optimization of scramjet inlet based on temperature and Mach number of supersonic combustion. *Aerosp. Sci. Technol.* **116**, 106864 (2021). <https://doi.org/10.1016/j.ast.2021.106864>
- Bezerra, I.S.A., Araújo, P.P.B., Souza, S.I.S., Marinho, G.S., Toro, P.G.P.: Influence of the hydrogen transverse injection mode in a scramjet combustor performance. *Int. J. Hydrogen Energy* **53**, 1269–1284 (2024). <https://doi.org/10.1016/j.ijhydene.2023.11.308>
- Capra, B.R., Brown, L.M., Boyce, R.R., Tirtey, S.C.: Aerothermal-structural analysis of a rocket-launched Mach 8 scramjet experiment: ascent. *J. Spacecr. Rocket.* **52**(3), 684–696 (2015). <https://doi.org/10.2514/1.A33112>
- Capra, B.R., Brown, L.M., Boyce, R.R.: Aerothermal-structural analysis of a rocket-launched Mach 8 scramjet experiment: descent. *J. Spacecr. Rocket.* **55**(2), 501–517 (2018). <https://doi.org/10.2514/1.A33964>
- Carandente, V., Scigliano, R.: Thermo-structural design of the Hexafly-INT Experimental Flight Test Vehicle (EFTV) and Experimental Service Module (ESM). In: 57th AIAA/ASCE/AHS/ASC Structures, Structural Dynamics, and Materials Conference, California, USA, AIAA 2016-1716. <https://doi.org/10.2514/6.2016-1716> (2016)
- Carneiro, R., Araújo, P.P.B., Marinho, G.S., Martos, J.F.A., Passaro, A., Toro, P.G.P.: Leading-to-trailing edge theoretical design of a generic scramjet. *AIP Adv.* **12**, 055322 (2022)
- Carneiro, R., Passaro, A., Toro, P.G.P.: Heat addition with variable area: methodology for preliminar design of the scramjet combustion chamber. *Phys. Fluids* **35**, 046103 (2023). <https://doi.org/10.1063/5.0138781>
- Celik, I.B., Ghia, U., Roache, P.J., Freitas, C.J.: Procedure for estimation and reporting of uncertainty due to discretization in CFD applications. *J. Fluids Eng.* **130**(7), 078001 (2008). <https://doi.org/10.1115/1.2960953>
- Culler, A.J., McNamara, J.J.: Fluid-thermal-structural modeling and analysis of hypersonic structures under combined loading. In: 52nd AIAA/ASME/ASCE/AHS/ASC Structures, Structural Dynamics

- and Materials Conference, Denver, Colorado, AIAA 2011-1965. <https://doi.org/10.2514/6.2011-1965> (2011)
- Gopinath, N.K., Jagadeesh, G., Basu, B.: Shock wave-material interaction in ZrB₂-SiC based ultra high temperature ceramics for hypersonic applications. *J. Am. Ceram. Soc.* **102**, 6925–6938 (2019). <https://doi.org/10.1111/jace.16548>
- Hank, J.M., Murphy, J.S., Mutzman, R.C.: The X-51A scramjet engine flight demonstration program. In: 15th AIAA International Space Planes and Hypersonic Systems and Technologies Conference, Dayton, Ohio, AIAA 2008-2540. <https://doi.org/10.2514/6.2008-2540> (2008).
- Heiser, W., Pratt, D.: Hypersonic Airbreathing Propulsion. AIAA Education Series, Washington (1994)
- Ho, S.-Y., Paull, A.: Coupled thermal, structural and vibrational analysis of a hypersonic engine for flight test. *Aerosp. Sci. Technol.* **10**, 420–426 (2006). <https://doi.org/10.1016/j.ast.2006.03.004>
- Martos, J.F.A.: Aerothermodynamic design, manufacturing and testing of a 3-D prototyped scramjet. Ph.D. thesis, Instituto Tecnológico de Aeronáutica (2017).
- MATWEB: Data sheets over 160000 metals, plastics, ceramics and composites. Material property data, <https://matweb.com/index.aspx> (2022). Accessed 30 September 2022.
- McClinton, C.R.: X-43 scramjet power breaks the hypersonic barrier Dryden lectureship in research for 2006. In: 44th AIAA Aerospace Sciences Meeting and Exhibit, Reno, Nevada, AIAA 2006-1. <https://doi.org/10.2514/6.2006-1> (2006)
- NASA, U.S.: Standard Atmosphere, 1976. National Oceanic and Atmosphere Administration, National Aeronautics and Space Administration, United States Air Force, Washington (1976)
- Oswatitsch, K.: Pressure recovery for missiles with reaction propulsion at high supersonic speeds (the efficiency of shock diffusers). Technical Memorandum, 1140, NACA (1947)
- Prakash, N.O., Venkatasubbaiah, K.: A new approach for the design of hypersonic scramjet inlets. *Phys. Fluids* **24**, 086103 (2012). <https://doi.org/10.1063/1.4748130>
- Ran, H., Mavris, D.: Preliminary design of a 2D supersonic inlet to maximize total pressure recovery. In: 5th Aviation, Technology, Integration, and Operations Conference (ATIO), Arlington, Virginia, AIAA 2005-7357. <https://doi.org/10.2514/6.2005-7357> (2005)
- Scigliano, R., Gardi, R.: Thermo-structural design of Ultra High Temperature Ceramic (UHTC) winglets of a re-entry space vehicle. In: 54th AIAA/ASME/ASCE/AHS/ASC Structures, Structural Dynamics, and Materials Conference, Boston, Massachusetts, AIAA 2013-1846. <https://doi.org/10.2514/6.2013-1846> (2013)
- Sung, C.J., Li, J.G., Yu, G., Law, C.K.: Chemical kinetics and self-ignition in a model supersonic hydrogen-air combustor. *AIAA J.* **37**, 208–214 (2012). <https://doi.org/10.2514/2.715>
- Sziroczak, D., Smith, H.: A review of design issues specific to hypersonic flight vehicles. *Prog. Aerosp. Sci.* **84**, 1–28 (2016). <https://doi.org/10.1016/j.paerosci.2016.04.001>
- Tavares, S., Hajela, P.: Thermal/structural dynamic analysis via approximate analytical approach. *Comput. Struct.* **43**(6), 1067–1073 (1992). [https://doi.org/10.1016/0045-7949\(92\)90007-M](https://doi.org/10.1016/0045-7949(92)90007-M)
- Tirtey, S.C., Boyce, R.R.: Generic axisymmetric scramjet thermal-structural analysis along a typical flight test trajectory. In: 16th AIAA/DLR/DGLR International Space Planes and Hypersonic Systems and Technologies Conference, AIAA 2009-7295. <https://doi.org/10.2514/6.2009-7295> (2012)
- Versteeg, H.K., Malalasekera, W.: An Introduction to Computational Fluid Dynamics: The Finite Volume Method. Pearson Education Limited, Harlow (2007)
- Volad, R.T., Huebner, L.D., McClinton, C.R.: X-43A hypersonic vehicle technology development. *Acta Astronaut.* **59**, 181–191 (2006). <https://doi.org/10.1016/j.actaastro.2021.07.030>
- Weber, B.J., MacKay, J.S.: Na analysis of ramjet engines using supersonic combustion. National Advisory Committee for Aeronautics, Technical note 4386, NACA TN 4386 (1958)

Publisher's Note Springer Nature remains neutral with regard to jurisdictional claims in published maps and institutional affiliations.

Springer Nature or its licensor (e.g. a society or other partner) holds exclusive rights to this article under a publishing agreement with the author(s) or other rightsholder(s); author self-archiving of the accepted manuscript version of this article is solely governed by the terms of such publishing agreement and applicable law.